ADVANCED FUNCTIONAL MATERIALS
www.afm-journal.de

Materials Views
www.MaterialsViews.com

Anion-Doped Mixed Metal Oxide Nanostructures Derived from Layered Double Hydroxide as Visible Light Photocatalysts

Seungho Cho, Ji-Wook Jang, Ki-jeong Kong, Eun Sun Kim, Kun-Hong Lee, and Jae Sung Lee**

Mixed metal oxide (MMO) nanostructures co-doped uniformly by carbon and nitrogen are synthesized for the first time by annealing a terephthalate-intercalated layered double hydroxide (LDH) under ammonia gas flow. The interlayer gallery of LDH allows effective access of NH_3 and the carbon source to its crystal lattice for a uniform nitrogen and carbon doping. Such co-doped MMO exhibit significantly red-shifted absorption spectra to visible light region relative to pure MMO. Photoelectrochemical water oxidation and incident-photon-to-current-conversion efficiency of LDH-derived photocatalysts demonstrate that all the visible light absorption caused by the anion doping contributes to the photocatalytic activity over the entire absorbed wavelength range of <610 nm. Density functional theory calculations of electronic structures are performed to elucidate the possibility of bandgap narrowing upon nitrogen and carbon co-doping on MMO structures.

1. Introduction

The world population and the demand for energy are increasing. Fossil fuels, the main energy source in the current energy system, are in limited supply, and their combustion produces carbon dioxide, the most important greenhouse gas. This situation has driven general interest in the development of alternative energy sources. Among the candidate technologies, solar energy conversion has the unique potential to meet the ever-growing energy demands in an environmentally benign manner.[1,2] With an average flux at about 160 W m^{-2}, solar radiation reaching the Earth's surface offers energy at a rate that is orders-of-magnitude larger than the rates provided by other primordial energy sources such as geothermal gradient, atmospheric electric discharge, and radioactivity.[1,3]

Metal oxide nanostructures are promising materials for the solar energy conversion. They are highly stable, their small size is comparable to their carrier scattering length, they display strong absorption coefficients due to an increased oscillator strength, and their synthetic routes are well-established.[4] Among the metal oxides, zinc oxide (ZnO, space group = $P6_3mc$; a = 0.32495 nm, c = 0.52069 nm) is useful for photocatalysis, photoelectrochemical processes and photovoltaics.[5] It assumes a very rich variety of nanostructures.[6] The energy levels for the conduction and valence bands, and the electron affinity of ZnO are similar to those of titanium dioxide (TiO_2), which is the best-studied photocatalyst or photoelectrode.[7] However, ZnO provides much higher electron mobility (205–1000 cm^2 V^{-1} s^{-1}) than that of TiO_2 (0.1–4 cm^2 V^{-1} s^{-1}),[8] thereby enhancing the electron transfer efficiency. There have been several reports for ZnO displaying more impressive photocatalytic activity than TiO_2.[9–12] In addition, ZnO nanostructures have low production costs compared to other binary metal oxide nanostructures.

The solar energy-conversion process using metal oxides involves the absorption of photons to induce electron-hole separations in their energy bands. An Achilles' heel of wide bandgap metal oxides such as ZnO (E_g = 3.37 eV for bulk ZnO) is that they do not absorb significantly light in the visible region of the solar spectrum due to their deep valence band positions. Visible light accounts for 44–47% of the solar energy spectrum, whereas UV light accounts for only 3–5%. Efficient use of visible light, therefore, is an essential prerequisite for the efficient use of solar energy.

Several approaches have been developed in an effort to overcome this limitation of wide bandgap metal oxides,[13] and one of them is the substitutional doping. Bandgap narrowing can be achieved by either elevating the valence band maximum (VBM) or lowering the conduction band minimum (CBM). For a spontaneous photoelectrochemical (PEC) water-splitting process, the band edge alignment is also important because chemical potentials of the oxidation and hydrogen production reactions must lie between the VBM and CBM. The CBM energy of ZnO is just slightly above the hydrogen production level and VBM is

Dr. S. Cho, Dr. J.-W. Jang, E. S. Kim, Prof. K.-H. Lee, Prof. J. S. Lee
Department of Chemical Engineering
Division of Advanced Nuclear Engineering
Pohang University of Science and Technology (POSTECH)
San 31, Hyoja-dong, Pohang, 790-784, South Korea
E-mail: ce20047@postech.ac.kr; jlee@postech.ac.kr
Dr. K.-j. Kong
Korea Institute of Chemical Technology
100 Jang-dong, Yuseong-gu, Daejeon, 305-343, South Korea

DOI: 10.1002/adfm.201201883

far below the water oxidation energy level.[14] Thus, it is necessary to narrow its bandgap by elevating the VBM while maintaining the CBM unaltered.[15] Metal doping can lead to CBM lowering. In contrast, in the case of anion doping with C or N, the VBM can be elevated by formations of hybridized orbitals of O 2p states and C or N 2p states,[16] and/or the localized states of C 2p or N 2p may be generated within the bandgap,[17] since the C 2p and N 2p states have higher orbital energies than the O 2p state, while keeping the CBM almost unaltered.

In the case of carbon-doping in ZnO, unintentional doping during the synthetic processes, such as metal-organic chemical vapor deposition[18,19] or pulsed laser deposition[20] has been reported. In addition, calcination of zinc-oxygen-carbonaceous species nanocomposites have been conducted to synthesize carbon-doped ZnO nanostructures.[21] However, these approaches require very limited synthetic conditions and are hard to control properties of the products. In contrast, nitrogen doping was realized mainly by the post-treatment such as N_2 or N_2O plasma treatments[22] and thermal treatments in N_2O or NH_3 atmosphere.[23,24] These post-treatment methods have two sides to consider. The approach can be applied to a number of ZnO structures already-synthesized by various synthetic methods. However, in general, dopants in the materials incorporated by the post-treatments are distributed mainly within the subsurface region of a very limited depth.[25] Significant limitations are caused by this non-uniform dopant distribution, such as limited visible-light absorbance and lowered mobility of carriers in the localized states, which deteriorate the visible-light photocatalytic activity.[16,25] Thus, if one can find a way to distribute the dopant more uniformly over the entire crystal structure, it could open up more opportunities to take advantage of the effective substitutional doping to tune optical and electrical properties of semiconductor oxides for various solar conversion applications.

Herein we report for the first time a strategy for an effective anion-doping of metal oxide nanostructures using layered double hydroxide (LDH) nanostructures as precursors. The LDHs, also known as anionic clays or hydrotalcite-like compounds, are an important class of ionic lamellar solids.[26] The general formula of LDHs is $[M^{II}_{(1-x)}M^{III}_{(x)}(OH)_2][A^{m-}_{x/m}\cdot nH_2O]$ (M^{II} = Zn, Mg, Co, Ni, Fe; M^{III} = Al, Cr, Ga; A = CO_3^{2-}, Cl^-, NO_3^-, CH_3COO^-).[27] The LDHs have the following noticeable features that allow the rational design of synthetic strategy: i) A wide variety of M^{II} and M^{III} ions can be adopted to tune their properties. ii) Positively charged metal hydroxide layers are balanced by intercalation of interlayer anions of choice. iii) LDHs can be converted to mixed metal oxide (MMO) structures by heat treatments. The MMO structures synthesized in this study, zinc aluminum MMOs, are based on ZnO and contain zinc aluminum oxide ($ZnAl_2O_4$, space group = *Fd3m*; a = 0.80872 nm, E_g = 3.8 eV for bulk). Thus, terephthalate-intercalated zinc aluminum layered double hydroxide (ZnAl:LDH) nanostructures as precursors were synthesized and then heat-treated under ammonia gas flow to obtain anion (N,C)-doped zinc aluminum MMO nanostructures. The interlayer gallery of LDH allowed effective access of NH_3 and the carbon source to its crystal lattice for a uniform carbon and nitrogen doping. Such well-doped MMO exhibited significantly red-shifted absorption spectra to visible light region relative to pure MMO. PEC water oxidation and incident-photon-to-current-conversion efficiency (IPCE) measurements demonstrated that all the visible light absorption brought by the anion doping contributed to the photoactivity over the entire absorbed wavelength range of <610 nm. This work also represents the first application of LDH-derived photocatalysts to photoelectrochemical water spliting.

2. Results and Discussion

2.1. Synthesis and Characterization of Anion-Doped Mixed Metal Oxide Nanostructures Derived from Layered Double Hydroxides

ZnAl:LDH nanostructures were chosen as a precursor for synthesizing visible light-active photocatalysts by anion doping of metal oxides. Three salient features of LDHs attracted our attention as mentioned briefly in the Introduction part. The LDHs consist of structures similar to the brucite structure, $Mg(OH)_2$, in which each Mg^{2+} ion is surrounded by six OH^- ions in an octahedral arrangement. LDHs are obtained when a fraction of the divalent cations (Zn^{2+} in our case) are isomorphously replaced by trivalent cations (Al^{3+} in our case) as illustrated in **Figure 1**A. The existence of the trivalent cations with

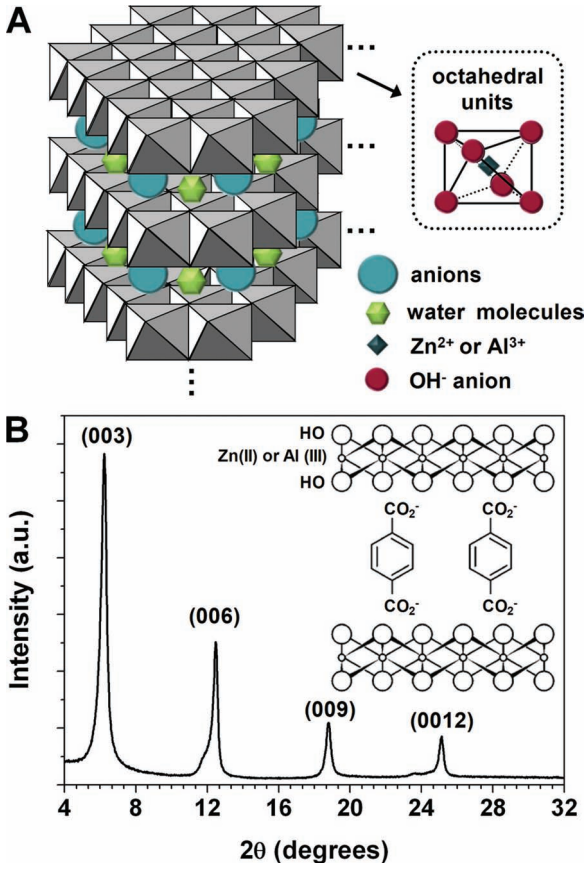

Figure 1. A) Schematic diagram of the ZnAl:LDH structures. B) XRD pattern of the powders synthesized from the reaction with an aqueous solution containing 0.3 M zinc nitrate hexahydrate, 0.1 M aluminum nitrate nonahydrate, 0.1 M terephthalic acid, and 0.8 M sodium hydroxide at 75 °C for 48 h.

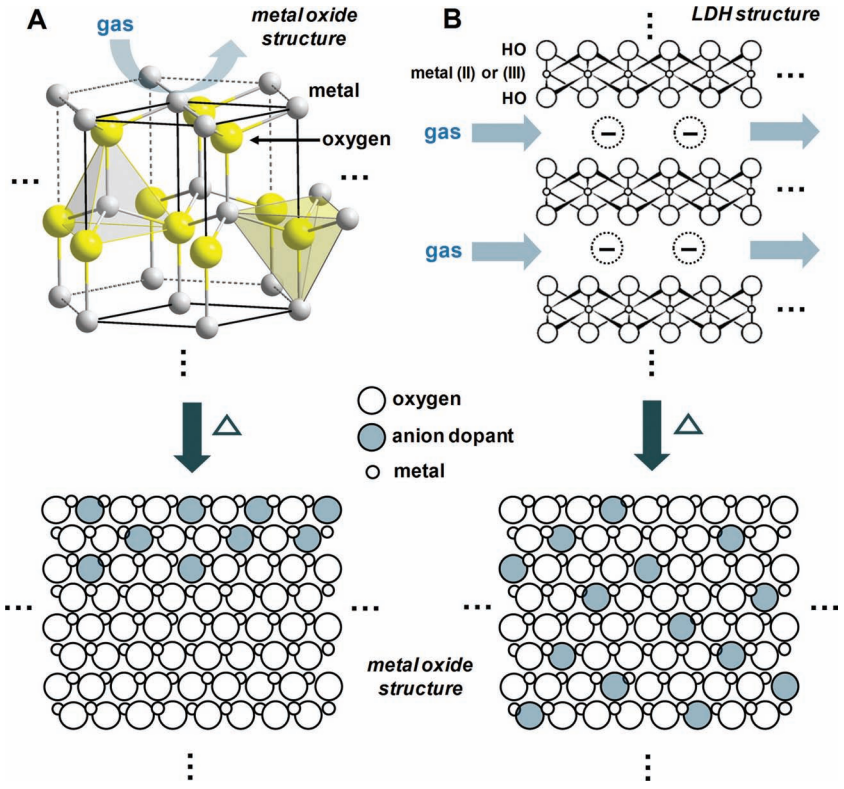

Figure 2. Schematic diagram showing access of a nitriding gas to the precursors in the cases of A) bulk ZnO structure and B) ZnAl:LDH structure.

higher charge gives rise to an overall positive charge in the brucite-type layers, which is balanced by intercalation of interlayer anions. Thus, the first structural feature of LDH that should be highlighted is that it has the galleries between the brucite-type layers. The second feature is that the interlayer anions between the brucite-type layers can be chosen or exchanged by the common intercalation chemistry.[28] The anions may be organic or inorganic, simple or complex.[29] The third feature is that each layer of LDH could be easily moved and reconstructed under applied energy.[30,31] Generally, LDH is converted to MMO by a heat treatment. In the case of ZnAl:LDH with no catalytic activity, heat treatments result in formation of MMO composed of ZnO and $ZnAl_2O_4$ with photocatalytic activities.

ZnAl:LDH nanostructures intercalated with terephthalate anions were prepared by addition of terephthalic acid to the precipitation solution. The XRD pattern of synthesized powders (Figure 1B) was typical of hydrotalcite-like materials, exhibiting (00*l*) reflections. The diffraction peaks were indexed based on rhombohedral symmetry (the $3R_1$ polytype). Four (00*l*) basal reflections as a series of equispaced peaks were observed and the value of d_{003} was 1.458 nm, corresponding to a gallery height of 0.982 nm. The space occupied by a terephthalate anion when intercalated with its long axis perpendicular to the host layers is predicted to be 0.98–1.01 nm,[32,33] which is consistent with the value of the gallery height of our LDH powders.

As illustrated in **Figure 2**A, in the case of a nitration of bulk metal oxide (e.g., ZnO) with a gaseous species (the conventional anion doping method), the gaseous species influences only subsurface region of a limited depth even if they have a thin, plate morphology. In contrary, LDH (e.g., ZnAl:LDH) has interlayer galleries between the two dimensional brucite-type sheets, which is expected to offer an efficient pathway for the nitriding gas as illustrated in Figure 2B. In addition, the interlayer anions of our precursors are terephthalates, which provides a situation similar to the zinc-oxygen-carbonaceous species composites used as precursors to carbon-doped ZnO nanostructures by heat treatments.[21] Therefore, the ZnAl:LDH nanostructures intercalated by terephthalates are expected to be effective precursors for C and N co-doped MMO nanostructures by heat treatment in a nitriding gas. This process is expected to produce the doped MMO with dopants more uniformly distributed deep into the bulk. The ZnAl:LDH nanostructures intercalated with terephthalates were heat-treated under ammonia gas flow at 900 K for 5 h (their SEM image after the nitration is provided in the Supporting Information, Figure S1). Powder XRD analysis was conducted for the obtained product solid (**Figure 3**). The ZnAl:LDH peaks as seen in Figure 1B disappeared completely and new peaks emerged as a result of the heat treatment in the NH_3 gas. These new peaks could be indexed as a wurtzite ZnO phase (JCPDS No. 35-1451) as the dominant phase and a cubic $ZnAl_2O_4$ crystalline phase (JCPDS No. 05-0669), indicating that the crystalline phase of ZnAl:LDH was converted into ZnO (the dominant phase) and $ZnAl_2O_4$. Thus, ZnO-based MMO structures were synthesized under our synthetic condition.

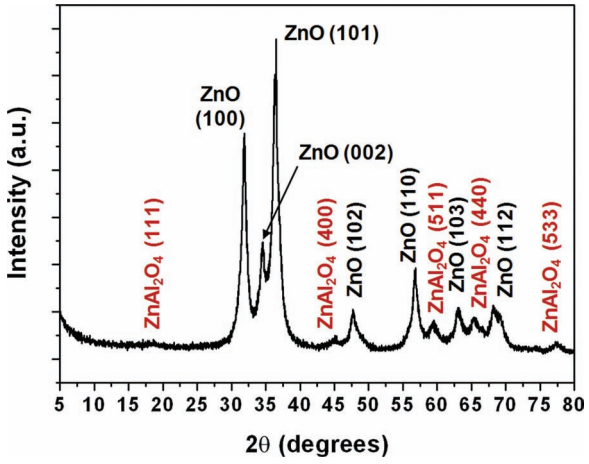

Figure 3. XRD pattern of the powders synthesized from the heat-treatment of ZnAl:LDH nanostructures intercalated with terephthalates under ammonia gas flow at 900 K for 5 h.

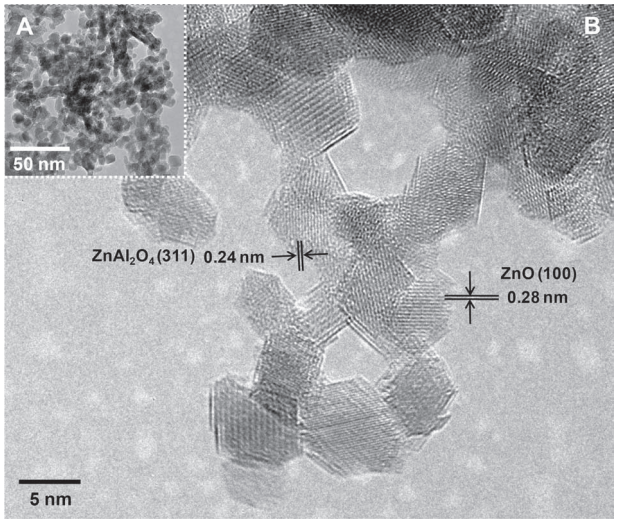

Figure 4. A,B) Low-magnified TEM image and HR-TEM image of the powders synthesized from the heat-treatment of ZnAl:LDH nanostructures intercalated with terephthalates under ammonia gas flow at 900 K for 5 h, respectively.

A low-magnification TEM image of the MMO nanostructures (**Figure 4**A) reveals that their structures are porous. A high-resolution TEM (HR-TEM) image (Figure 4B) shows that the MMO nanostructures are highly crystalline and crystal phases of ZnO and $ZnAl_2O_4$ co-exists, which is consistent with the result of XRD analysis. The crystal grains have lattice spacings of 0.24 nm and 0.28 nm, corresponding to the distance between the (311) planes in the $ZnAl_2O_4$ crystal lattice and that between the {100} planes in the ZnO crystal lattice, respectively. The nitrogen adsorption–desorption isotherm for the MMO nanostructures is shown in **Figure 5**A. A type-IV adsorption–desorption isotherm is observed, and such isotherm is usually associated with capillary condensation in mesopores.[34] The Barrett–Joyner–Halenda (BJH) method were used to calculate

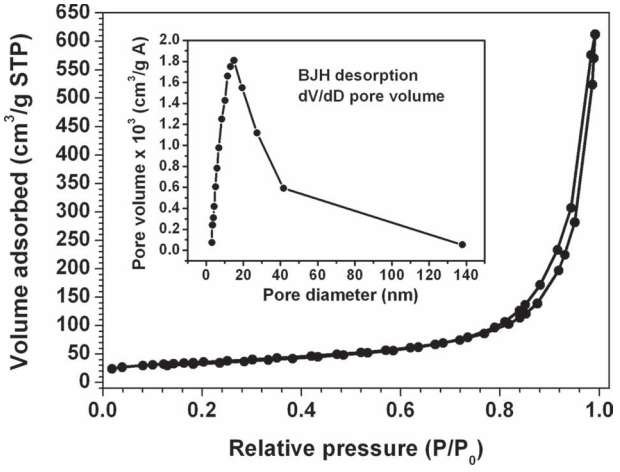

Figure 5. Nitrogen adsorption–desorption isotherms for the powders synthesized from the heat-treatment of ZnAl:LDH nanostructures intercalated with terephthalates under ammonia gas flow at 900 K for 5 h. The inset is the corresponding pore size distributions.

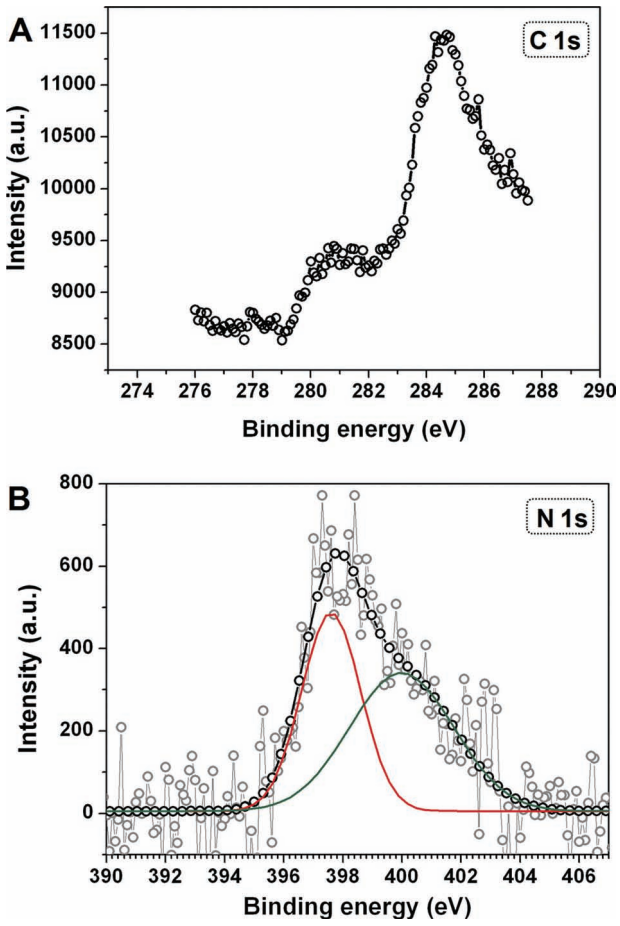

Figure 6. A) C 1s and B) N 1s XPS spectra of the powders synthesized from the heat-treatment of ZnAl:LDH nanostructures intercalated with terephthalates under ammonia gas flow at 900 K for 5 h.

the pore size distribution (Figure 5B), which indicated that the as-synthesized samples had a pore structure with strong peak centered at 16 nm. The BET surface area of the MMO nanostructures was 128.3 m^2/g.

Quantitative analysis using the elemental analyzer revealed that the MMO nanostructures contained 0.9 wt% carbon and 0.8 wt% nitrogen. We also performed XPS studies to investigate the states of the doped C and N atoms. As shown in **Figure 6**A (the core level spectrum in the C 1s region), two peaks centered at 281.1 and 284.8 eV were identified. The peak at 284.8 eV was attributed to graphite and/or carbon from contamination or a carbon tape for attaching samples for XPS analysis.[20] The lower binding energy peak suggested the presence of carbon atoms in a carbide form,[35] indicating the substitution of carbon for oxygen and the formation of O-(Zn or Al)-C bonds in the synthesized nanostructures. In the case of nitrogen, as shown in Figure 6B (the core level spectrum in the N 1s region), two peaks centered at 399.8 and 397.6 eV were identified by fitting the experimental line profile. The 399.8 eV is a typical value of the N 1s binding energy in amines,[36] presumably originated from the presence of N-H compounds due to incomplete decomposition of NH_3.[24] The peak at 397.6 eV is located between the typical binding energy for metal nitride (≈396–397 eV)[37] and NO

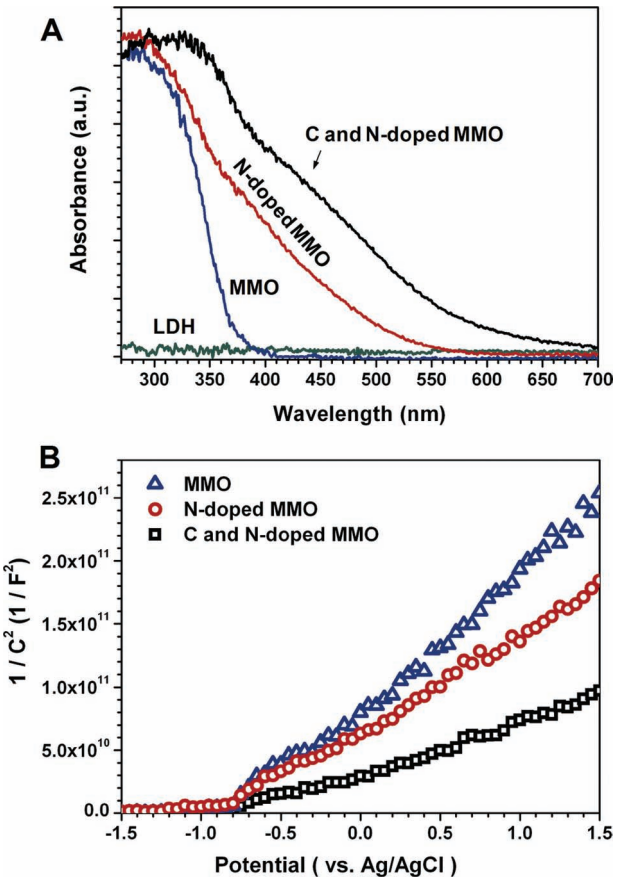

Figure 7. A) UV-vis absorption spectra of the ZnAl:LDH nanostructures, the MMO nanostructures, the N-doped MMO nanostructures and the C and N co-doped MMO nanostructures. B) Mott–Schottky plots of MMO, N-doped MMO and C and N co-doped MMO. The Mott–Schottky plots were measured in 0.5 M Na_2SO_4 solution.

type species (above 400 eV),[38] and thereby can be attributed to N 1s of oxynitride (O-(Zn or Al)-N).[38,39] These XPS results, therefore, reveal that C and N dopants were incorporated substitutionally at O sites in the MMO nanostructures.

2.2 Optical Properties and Photocatalytic Activity of Doped Mixed Metal Oxide Nanostructures

The UV-vis absorption spectra of the synthesized nanostructures are presented in **Figure 7**A. The ZnAl:LDH nanostructures absorbed neither UV nor visible light. Pure MMO nanostructures prepared by calcination of ZnAl:LDH nanostructures at 900 K for 5 h in air exhibited a strong UV adsorption band ($\lambda \leq$ 400 nm) characteristic of the wide bandgap ZnO and $ZnAl_2O_4$. As another reference photocatalyst, N-doped MMO nanostructures were synthesized from the heat treatment of ZnAl:LDH nanostructures without terephthalate intercalation at 900 K for 5 h under ammonia gas flow. The ZnAl:LDH nanostructures without terephthalates were prepared by reaction of an aqueous solution containing 0.01 M zinc nitrate hexahydrate, 0.0033 M aluminum nitrate nonahydrate and 0.35 M ammonia at room temperature for 24 h. The N-doped MMO nanostructures showed absorption in the visible region as well as in the UV region.

The spectrum of C and N co-doped MMO nanostructures obtained from the heat treatment of ZnAl:LDH nanostructures intercalated with terephthalate at 900 K for 5 h under ammonia gas flow, was further red-shifted as compared to that of the N-doped MMO nanostructures. The significant red-shift of the absorption spectrum for the C and N co-doped MMO nanostructure is different from the commonly observed small absorbance shoulder in anion-doped ZnO structures.[24] We performed a control test, in which as-synthesized ZnO samples with thin plate building blocks (10–20 nm thickness)[40] were annealed in NH_3 under the same conditions. This test was intended to highlight the importance of the LDH structure for effective doping, i.e., a layer structure with a gallery that allows the approach of the dopant gases deep into the structure lattice. The absorption spectrum of the product from the thermal treatment of the ZnO precursors with NH_3 exhibits only shoulder tail in the visible light region (Figure S2 in the Supporting Information). This weak shoulder spectrum represents the typical absorption spectrum when the doping treatment is conducted for a usual bulk oxide precursor. Thus, the significant red-shift of the absorption spectra of the anion-doped MMO nanostructures derived from LDH is attributed to the existence of the interlayer galleries that allows the contact of single layer of ZnAl:LDH with NH_3 and the carbon-rich interlayer anions of the LDH as a precursor.

To investigate the relative band positions of the synthesized MMO nanostructures, we measured flat band potentials (Figure 7B). The flat band potentials of electrodes were determined by the Mott–Schottky relation:[41] $1/C^2 = (2/e\varepsilon\varepsilon_0 N)[V_a - V_{fb} - kT/e]$, where C is the space charge layers capacitance, e is the electron charge, ε is the dielectric constant, ε_0 is the permittivity of vacuum, N is the the charge carrier density, V_a is the applied potential, and V_{fb} is the flat band potential. The flat band potential (V_{fb}) was determined by taking the x intercept of a linear fit to the Mott–Schottky plot, $1/C^2$, as a function of applied potential (V_a). As shown in Figure 7B, the flat band potentials thereby the conduction band positions of MMO, N-doped MMO, and C and N-doped MMO are almost the same. Based on the measured flat band potentials and optical bandgap energies, it is revealed that the VBMs are upshifted by the anion-doping achieved by the strategy discussed here. The slope of the Mott–Schottky plots was used to estimate the charge carrier density. The carrier densities of the anion-doped MMO (N doping: 1.8×10^{20} cm^{-3}, C and N co-doping: 3.5×10^{20} cm^{-3}) increased relative to that of pure MMO (1.3×10^{20} cm^{-3}) at frequency of 10 kHz. The estimated energy band structures of the materials were provided in Figure S3 in the Supporting Information based on the Mott–Schottky plots and Tauc plots.

The visible light activities of the synthesized anion-doped MMO nanostructures were evaluated by measuring photocurrent density accompanying photoelectrochemical (PEC) water splitting under visible light ($\lambda \geq$ 420 nm). The PEC water splitting to produce hydrogen has been envisioned as a promising strategy for collecting the energy of sunlight and storing it in the form of chemical bonds.[42–45] Each MMO nanostructure

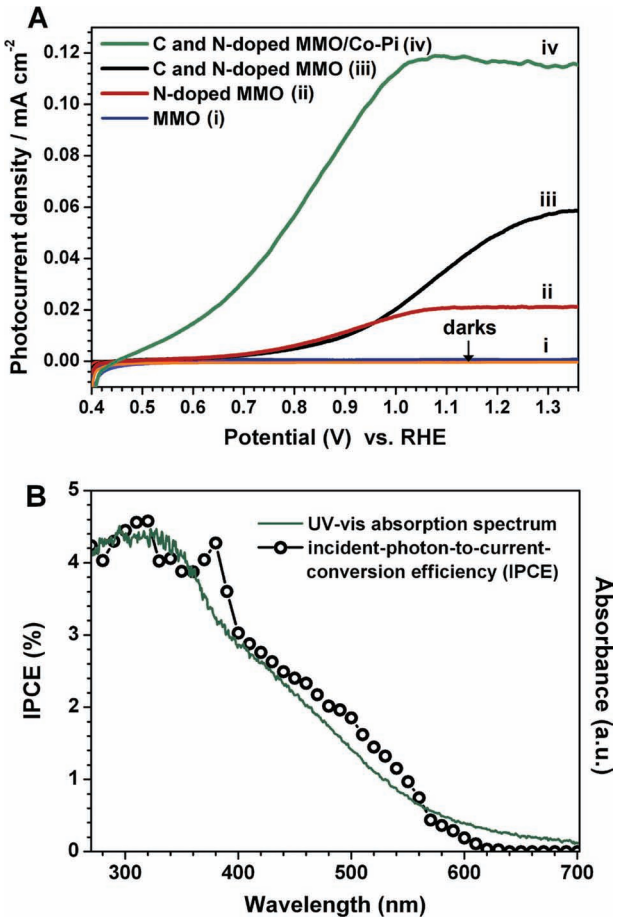

Figure 8. A) Photocurrent-potential curves for ZnAl:LDH nanostructures, the MMO nanostructures, the N-doped MMO nanostructures, the C and N co-doped MMO nanostructures, and the amorphous cobalt-phosphate (Co-Pi)-deposited C and N co-doped MMO nanostructures measured under a Xe-arc lamp (300 W) attached with a UV cut-off filter ($\lambda \geq$ 420 nm) in a 0.1 M pH 7 potassium phosphate buffer solution. B) Incident-photon-to-current-conversion efficiency (IPCE) of C and N co-doped MMO nanostructures measured at 1.23V vs. RHE and the corresponding UV-vis absorption spectrum.

synthesized in a powder form was loaded onto the fluorine-doped tin oxide (FTO) glass by using electrophoretic deposition (EPD) technique. **Figure 8**A shows a set of linear sweep voltammograms measured for the nanostructure photoanodes in a 0.1 M pH 7 potassium phosphate buffer solution under dark or under visible light. Linear sweep voltammetry is a common electrochemical technique for examining charge-carrier characteristics at a semiconductor/electrolyte interface.[46] The photocurrent observed under light illumination is a direct measure of the rate of water splitting and reflects the number of charge carriers produced from the incident light and their subsequent participation in the water oxidation reaction on the photoanode or hydrogen ion reduction on the counter electrode.[47] Visible light irradiation on photoanodes drives PEC water oxidation reactions to generate photoelectrons, which are collected by the FTO substrate to produce currents: $2H_2O\ (l) + h\nu \rightarrow O_2\ (g) + 4H^+ + 4e^-$.

All photoanodes showed negligible dark current densities. In the case of pure MMO nanostructure, small photocurrent (0.54 μA/cm^2) was produced at 1.23 V *vs.* RHE, presumably due to poor visible light absorption. Here we compare the photocurrent generation at 1.23 V vs. RHE, which is the theoretical potential necessary for water oxidation. The photocurrent increased by anion-doping. The photocurrent produced by N-doped MMO photoanodes is 0.021 mA/cm^2 at 1.23 V vs. RHE. The C and N co-doped MMO nanostructure photoanodes exhibited a 2.5-fold enhancement in the photocurrent density (0.053 mA) at 1.23 V vs. RHE, relative to N-doped MMO nanostructure photoanodes. These results may be attributed to the improved visible light absorption and increase of carrier density by C and N co-doping, as shown in the UV-vis absorption spectra (Figure 7A) and the Mott–Schottky plot (Figure 7B). In addition, a water oxidation catalyst was deposited on the C and N co-doped MMO photoanode. Recently, an amorphous cobalt-phosphate-based material (Co-Pi) was discovered that catalyzed water oxidation at relatively low overpotentials in pH 7 phosphate buffer.[45,48,49] Thus, Co-Pi was electrodeposited onto the C and N co-doped MMO photoanode in a solution containing 0.5 mM Co^{2+} and 0.1 M potassium phosphate buffered at pH 7. The Co-Pi deposition yields a cathodic shift of >150 mV in the photocurrent onset potential and a two-fold enhancement in the photocurrent density (0.116 mA) at 1.23 V vs. RHE. The photocurrent reached its saturation value quickly by showing the plateau from 1.0 V vs. RHE. The Co-Pi deposition facilitated the transfer of charge carrier generated on the photoanode as well as lowered the overpotential on the water oxidation reaction. Photogenerated holes in the C and N co-doped MMO nanostructures under visible light were promptly involved in the oxygen evolution cycle of Co-Pi, which led to efficient O_2 evolution with a reduction of charge recombination probability.[45] Thus, the synergetic effect of the Co-Pi as electrocatalyst and the uniformly anion-doped MMO from LDH structure gives an excellent behavior of C and N co-doped MMO/Co-Pi as a photoanode.

To examine the stability of photocurent generated by C and N co-doped MMO/CoPi, a constant potential measurement was performed at 1.23 vs. RHE (Figure S4, Supporting Information). A steady photocurrent around 0.10 mA/cm^2 was persisted for as long as 100 min and amounts of evolved hydrogen during this period was 2.8 μmol. This value is about 90% of the one expected by the net photocurrent (3.1 μmol), and represents the faradaic efficiency of the system. This indicates that the photo-generated and collected charges are successfully used for water splitting.

IPCE measurements were conducted to further study the photoresponse of the anion-doped MMO photoanode as a function of the wavelength of incident light (Figure 8B). The IPCE is defined by the following equation:IPCE = $[J\ 1240]/[P_{mono}\lambda]$, where J is the photocurrent density (mA/cm^2), P_{mono} is the light power density (mW/cm^2) at λ, and λ is the wavelength of incident light (nm). The IPCE over the entire UV-visible region was below 5%. To enhance the IPCE values, we believe that the system needs further optimization particularly in terms of connectivity between MMO particles (see Figure S5 in the Supporting Information), which is essential for high efficiency.[50] In any case, it is interesting that the IPCE curve traces almost

exactly the absorbance curve. This indicates that all the photons (even with the longest wavelength) absorbed by the visible light absorbing sites created by the C and N co-doping contribute to water oxidation. This is unusual because non-uniform dopant distribution in conventional doping treatments offers limited visible-light absorbance, lowered mobility of carriers in the localized states, and defect sites for facile charge recombination, which deteriorate the visible-light photocatalytic activity.[16,25] Thus, to the best of our knowledge, there has been no report on anion-doped zinc oxide or zinc aluminum oxide, which shows photocatalytic activity all the way to 610 nm. Even in the case of narrow bandgap metal oxide photocatalysts which absorb the visible light such as Fe_2O_3[51] and $CaFe_2O_4$,[52] the photocurrent is very low compared with their absorption in the wavelength longer than 500 nm. This proves that using LDH as a precursor to doped-MMO is an effective strategy because dopant gas can utilize the galleries between the layers to approach directly the doping reaction sites.

To elucidate the possibility of bandgap narrowing upon nitrogen and carbon doping on MMO structures, we performed density functional theory (DFT) calculations of electronic structures. For simplicity, we assumed MMO structures as wurtzite ZnO structures, which is the dominant crystalline phase under our synthetic conditions. Our calculations are based on spin-polarized Kohn-Sham theory with the generalized gradient approximation and the projector augmented wave potentials as implemented in the Vienna ab initio simulation package code.[53] It is known that the conventional DFT method always underestimates the bandgap of semiconductors. The calculated bandgap using DFT is only 0.76 eV, compared to the experimental value of 3.2 eV. In spite of this error, the qualitative trend of bandgap changes can be well assigned. The calculated total density of states (TDOS) and partial density of states (PDOS) at each configuration in stable structure are shown in **Figure 9**. Since the 2p orbital of the N atom is similar to O 2p, the p-d coupling between dopant N and Zn results in the valence band edge position close to that of the host system (ZnO). However, the energy of N 2p orbital is 2.9 eV higher than that of the O 2p orbital and N substitution increases the valence band energy. As shown in Figure 9B, occupied N-derived defect band appears just above the VBM of the ZnO host system with a bandwidth of 0.3 eV. The PDOS analysis indicates that this defect band involves coupling between N 2p and Zn 3d states, which is higher in energy than the valence band mainly composed of O 2p and Zn 3d states, and the oxygen states have little contribution to this defect band. The energy gap between this defect band and CBM is only 0.56 eV. In the case of C and N doped ZnO, the bandgap is further narrowed (Figure 9C). These calculation results are in agreement with our experimental results. We also investigated the redistribution of the charge density upon doping by plotting the electron density difference, (i.e., ρ(C and N doped ZnO)–ρ(undoped ZnO)), as shown in Figure S6 in the Supporting Information. The positive and negative regions of the electron density difference are shown in yellow and cyan colors. Because C and N have smaller number of electrons compared to O atom, the charge deficiency is mainly occurred around the dopant atoms. Small amount of charge buildup occurs between dopant and Zn atoms, which is responsible for the occupied defect states, which narrows bandgap as shown in Figure 9.

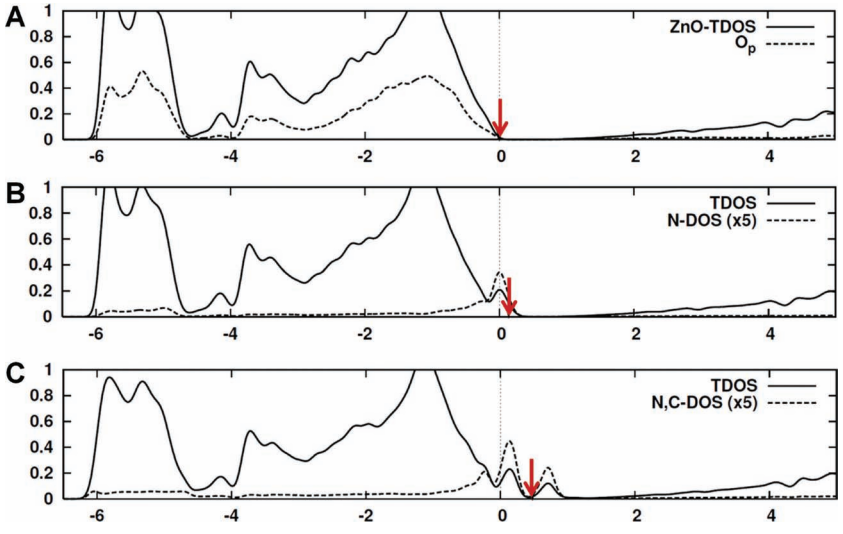

Figure 9. Calculated TDOS and PDOS (sum of spin-up and spin-down DOS) of A) undoped ZnO, B) N-doped ZnO, and C) C and N doped ZnO. Here the comparisons are made by aligning the 2s orbital of oxygen and taking as zero the energy of the valence band maximum of the undoped ZnO. The arrows indicate Fermi level in each configuration.

3. Conclusions

We presented a fruitful strategy for effective incorporation of dopant anions in MMO crystal structures by using LDH as a precursor. This designed method induced direct access of carbon and nitrogen precursors to metal oxide crystal lattice, using the features of LDH nanostructures, i.e., each LDH layer is accessible through the interlayer galley. The uniformly anion-doped MMO nanostructures prepared by this strategy absorbed visible light exhibiting significant red-shift of absorption spectra mainly due to the up-shift of VBM. It was demonstrated that all the visible light absorption brought by the anion doping contributed to the photocatalytic activity over the entire absorbed wavelength range. Thus even 610 nm photons showed photocatalytic water splitting activity on MMO. The elevation of VBM upon anion doping (C and N) was verified by DFT calculations. These results warrant efforts to extend this strategy to synthesize other anion-doped MMO nanostructures in general with different combinations of divalent-trivalent cations using various LDH nanostructures. We also expect that this strategy of effective doping could open up the way to tune optical and electrical properties of MMO nanostructures to obtain high photocatalytic activity under visible light.

4. Experimental Section

Synthesis of ZnAl:LDH and Anion-Doped Zinc Aluminum MMO Nanostructures: All chemicals

used in this study were of analytical grade and were used without further purification. ZnAl:LDH nanostructures were synthesized by modifying the method reported by Gago et al.[30] An aqueous solution containing 0.3 M zinc nitrate hexahydrate ($Zn(NO_3)_2{\cdot}6H_2O$, 99%, Samchun), 0.1 M aluminum nitrate nonahydrate ($Al(NO_3)_3{\cdot}9H_2O$, 99%, Kanto Chemical), 0.1 M terephthalic acid ($C_6H_4(COOH)_2$, 98%, Aldrich) and 0.8 M sodium hydroxide (NaOH, 98%, Aldrich) was prepared and the solution was maintained at 75 °C for 48 h. After the reaction, the solution was filtered through a polycarbonate membrane filter (Isopore). The filtered powders were washed several times with deionized water and dried in an oven at 60 °C for 12 h. The as-prepared terephthalate-intercalated ZnAl:LDH powders were placed in a furnace and maintained at 900 K for 5 h under ammonia gas flow (100 cc/min), and then maintained at 773 K for 2 h in air to remove organic contaminants from the synthesized nitrogen and carbon co-doped zinc aluminum MMO nanostructures.

Characterization: The morphology, crystallinity, chemical composition, chemical states of the elements, and optical properties of the synthesized materials were determined using field-emission scanning electron microscopy (FESEM, JEOL JMS-7401F, operated at 10 keV), high-resolution scanning transmission electron microscopy (Cs-corrected HR-STEM, JEOL JEM-2200FS with an energy-dispersive X-ray spectrometer operating at 200 kV, National Center of Nanomaterials Technology (NCNT)), X-ray diffraction (XRD, Mac Science, M18XHF), elemental analysis (Analysennsysteme GmBH, Vario EL II), X-ray photoelectron spectroscopy (XPS, VG Scientific, EscaLab 200iXL), and UV-Vis diffuse reflectance spectroscopy (Shimadzu, UV2501PC). Nitrogen adsorption–desorption isotherms were measured at –196 °C using a Micromeritics analyzer (ASAP 2020 V3.01 H analyzer).

Photoanode Fabrication: Photoanodes were produced by using electrophoretic depositon (EPD) technique. Thus, 48 mg of MMO nanostructure powders and 12 mg of iodine were added to 30 mL of acetone, sonicated for 5 min, and stirred for 30 min to form a stable suspension. EPD was performed onto 1×1 cm^2 area of clean fluorine-doped tin oxide (FTO) glass (Pilkington, TEC 8, ≈8 Ω/square) substrate at 30 V for 5 min with another clean FTO glass as the counter electrode. The MMO- deposited FTO glass was washed with absolute alcohol, sintered in a furnace at 400 °C for 30 min in the air, and cooled to room temperature. And then copper wires were attached with silver paste to make the electrical connections. Finally the uncoated FTO surface was covered with epoxy resin. Cobalt phosphate (Co-Pi) was electrodeposited onto the C and N-doped MMO electrode at 1.0 V (vs. Ag/AgCl) in 0.5 mM cobalt nitrate and a 0.1 M potassium phosphate (KPi) pH 7 buffer solution.

Photoelectrochemical (PEC) Measurements: The current–potential (*I–V*) curve of PEC water oxidation were obtained in a 0.1 M pH 7 KPi buffer solution using a platinum foil counter electrode, a Ag/AgCl (3 M NaCl) reference electrode and a potentiostat (Potentiostat/Galvanostat Model 263A EG&G Princeton Applied Research). Prior to a measurement, the solution was purged with nitrogen for 30 min. The back side of photoanodes was illuminated with a Hg lamp (450 W, Oriel) attached with a UV cut-off filter ($\lambda \geq 420$ nm). The evolved amounts of H_2 were analyzed by a gas chromatograph (HP5890) with a thermal conductivity detector (TCD) and a molecular sieve 5-A column. Incident-photon-to-current-conversion efficiency (IPCE) was measured using a Hg lamp (450 W, Oriel) and a monochromator with a bandwidth of 5 nm. The IPCE was measured at 1.23 V (vs. RHE). Mott–Schottky analysis was carried out at a DC potential range –1.5 to 1.5 V vs. Ag/AgCl with the AC potential frequency 10 kHz and the amplitude of AC potential 0.050 V under dark condition.

Density Functional Theory (DFT) Calculations of Electronic Structures: The impurity calculations were carried out using $3 \times 3 \times 2$ wurtzite ZnO supercell geometry containing 72 atoms. We used a kinetic energy cutoff of 400 eV for the plane-wave expansions, and a $2 \times 2 \times 2$ mesh of special *k*-points for integrations over the Brillouin zone. We have examined many configurations, nitrogen or carbon atom substitution and also co-doping of N and C. In the case of two dopants, nearest neighbor pair substitution is more stable than far apart pair, the binding energy of pair substitution is 0.24 eV for N, 0.60 eV for C and 0.30 eV for co-doping. The stabilization of nearest neighbor pair of dopants is due to the charge compensation mechanism.[54] In order to get self-consistent results, we optimized lattice constants and atomic coordinates, which were obtained by minimizing the total energy, internal stress, and atomic forces. The convergence criteria for DFT calculations are 10^{-6} eV of total energy and 10^{-2} eV/Å of force.

Supporting Information

Supporting Information is available from the Wiley Online Library or from the author.

Acknowledgements

S.C. and J.-W.J. contributed equally to this work. This work was supported by grants from the BK21/WCU programs and Basic Science Research Program (No. 2012-017247) of the Ministry of Education of Korea, the Korea Science and Engineering Foundation (KOSEF) grant funded by the Korea government (MEST) (2011-0000360 and R31-30005), Hydrogen Energy R&D Center and the Korea Center for Artificial Photosynthesis (KCAP) funded by the MEST through the National Research Foundation of Korea (No. 2012M1A2A2671779). S.C. and J.-W.J. are grateful to Hyun Jin Park (researcher at NCNT) for TEM analysis.

Received: July 7, 2012
Revised: November 12, 2012
Published online: December 16, 2012

[1] V. I. Vullev, *J. Phys. Chem. Lett.* **2011**, *2*, 503.
[2] H. B. Gray, *Nat. Chem.* **2009**, *1*, 7.
[3] B. Sørensen, *Energy Policy* **1991**, *19*, 386.
[4] S. Cho, J.-W. Jang, S.-H. Lim, H. J. Kang, S.-W. Rhee, J. S. Lee, K.-H. Lee, *J. Mater. Chem.* **2011**, *21*, 17816.
[5] C. A. K. Gouvêa, F. Wypych, S. G. Moraes, N. Durán, N. Nagata, P. Peralta-Zamora, *Chemosphere* **2000**, *40*, 433.
[6] S. Cho, S.-H. Jung, K.-H. Lee, *J. Phys. Chem. C* **2008**, *112*, 12769.
[7] L.-C. Chen, Y.-J. Tu, Y.-S. Wang, R.-S. Kan, C.-M. Huang, *J. Photochem. Photobiol., A* **2008**, *199*, 170.
[8] Q. F. Zhang, C. S. Dandeneau, X. Y. Zhou, G. Z. Cao, *Adv. Mater.* **2009**, *21*, 4087.
[9] A. Akyol, H. C. Yatmaz, M. Bayramoglu, *Appl. Catal., B* **2004**, *54*, 19.
[10] N. Daneshvar, D. Salari, A. R. Khataee, *J. Photochem. Photobiol., A* **2004**, *162*, 317.
[11] M. C. Yeber, J. Rodriguez, J. Freer, J. Baeza, N. Duran, H. D. Mansilla, *Chemosphere* **1999**, *39*, 10.
[12] A. A. Khodja, T. Sehili, P. J. F. Ihichowski, P. Boule, *J. Photochem. Photobiol., A* **2001**, *141*, 231.
[13] a) J. Z. Zhang, *MRS Bull.* **2011**, *36*, 48; b) T. F. Jaramillo, S.-H. Baeck, A. Shwarsctein, K.-S. Choi, G. D. Stucky, E. W. McFarland, *J. Comb. Chem.* **2005**, *7*, 264.
[14] a) Y. H. Lu, S. P. Russo, Y. P. Feng, *Phys. Chem. Chem. Phys.* **2011**, *13*, 15973; b) Y. Q. Gai, J. B. Li, S. S. Li, J. B. Xia, S. H. Wei, *Phys. Rev. Lett.* **2009**, *102*, 036402.
[15] H. J. Zhang, G. H. Chen, D. W. Bahnemann, *J. Mater. Chem.* **2009**, *19*, 5089.
[16] R. Asahi, T. Morikawa, T. Ohwaki, K. Aoki, Y. Taga, *Science* **2001**, *293*, 269.
[17] H. Irie, Y. Watanabe, K. Hashimoto, *J. Phys. Chem. B* **2003**, *107*, 5483.
[18] S. T. Tan, X. W. Sun, Z. G. Yu, P. Wu, G. Q. Lo, D. L. Kwong, *Appl. Phys. Lett.* **2007**, *91*, 072101.

[19] X. Li, S. E. Asher, S. Limpijumnong, S. B. Zhang, S.-H. Wei, T. M. Barnes, T. J. Coutts, R. Noufi, *J. Vac. Sci. Technol., A* **2006**, *24*, 1213.
[20] H. Pan, J. B. Yi, L. Shen, R. Q. Wu, J. H. Yang, J. Y. Lin, Y. P. Feng, J. Ding, L. H. Van, J. H. Yin, *Phys. Rev. Lett.* **2007**, *99*, 127201.
[21] S. Cho, J.-W. Jang, J. S. Lee, K.-H. Lee, *CrystEngComm* **2010**, *12*, 3929.
[22] T. M. Barnes, J. Leaf, S. Hand, C. Fry, C. A. Wolden, *J. Appl. Phys.* **2004**, *96*, 7036.
[23] G. D. Yuan, W. J. Zhang, J. S. Jie, X. Fan, J. A. Zapien, Y. H. Leung, L. B. Luo, P. F. Wang, C. S. Lee, S. T. Lee, *Nano Lett.* **2008**, *8*, 2591.
[24] X. Yang, A. Wolcott, G. Wang, A. Sobo, R. C. Fitzmorris, F. Qian, J. Z. Zhang, Y. Li, *Nano Lett.* **2009**, *9*, 2331.
[25] G. Liu, L. Wang, C. Sun, X. Yan, X. Wang, Z. Chen, S. C. Smith, H.-M. Cheng, G. Q. Lu, *Chem. Mater.* **2009**, *21*, 1266.
[26] V. Rives, *Layered Double Hydroxides: Present and Future*, Nova Science Publishers, Inc., New York **2001**.
[27] F. Cavani, F. Trifirò, A. Vaccari, *Catal. Today* **1991**, *11*, 173.
[28] A. I. Khan, D. O'Hare, *J. Mater. Chem.* **2002**, *12*, 3191.
[29] V. Rives, M. A. Ulibarri, *Coord. Chem. Rev.* **1999**, *181*, 61.
[30] X. Zhao, F. Zhang, S. Xu, D. G. Evans, X. Duan, *Chem. Mater.* **2010**, *22*, 3933.
[31] S. Cho, K.-H. Lee, *J. Alloys Compd.* **2011**, *509*, 8770.
[32] S. Gago, M. Pillinger, T. M. Santos, I. S. Gonçalves, *Ceramics–Silikáty* **2004**, *48*, 155.
[33] Z. P. Xu, H. C. Zeng, *J. Phys. Chem. B* **2000**, *104*, 10206.
[34] K. S. W. Sing, D. H. Everett, R. A. W. Haul, L. Moscou, R. A. Pierotti, J. Rouquerol, T. Siemiemewska, *Pure Appl. Chem.* **1985**, *57*, 603.
[35] L. Ramqvist, K. Hamrin, G. Johansson, A. Fahlman, C. Nordling, *J. Phys. Chem. Solids* **1969**, *30*, 1835.
[36] V. Musat, A. M. Rego, R. Monteiro, E. Fortunato, *Thin Solid Films* **2008**, *516*, 1512.
[37] K. Toyoura, H. Tsujimura, T. Goto, K. Hachiya, R. Hagiwara, Y. Ito, *Thin Solid Films* **2005**, *492*, 88.
[38] Y. Yan, S. B. Zhang, S. T. Pantelides, *Phys. Rev. Lett.* **2001**, *86*, 5723.
[39] J. M. Bian, X. M. Li, X. D. Gao, W. D. Yu, L. D. Chen, *Appl. Phys. Lett.* **2004**, *84*, 541.
[40] S. Cho, J.-W. Jang, J. S. Lee, K.-H. Lee, *Langmuir* **2010**, *26*, 14255.
[41] F. Cardon, W. P. Gomes, *J. Phys. D: Appl. Phys.* **1978**, *11*, L63.
[42] A. Heller, *Science* **1984**, *223*, 1141.
[43] M. Grätzel, *Nature* **2001**, *414*, 338.
[44] N. S. Lewis, D. G. Nocera, *Proc. Natl. Acad. Sci. USA* **2006**, *103*, 15729.
[45] D. K. Zhong, D. R. Gamelin, *J. Am. Chem. Soc.* **2010**, *132*, 4202.
[46] A. Wolcott, W. A. Smith, T. R. Kuykendall, Y. Zhao, J. Z. Zhang, *Small* **2009**, *5*, 104.
[47] Y.-S. Hu, A. Kleiman-Shwarsctein, A. J. Forman, D. Hazen, J.-N. Park, E. W. McFarland, *Chem. Mater.* **2008**, *20*, 3803.
[48] M. W. Kanan, D. G. Nocera, *Science* **2008**, *321*, 1072.
[49] Y. Surendranath, M. Dincă, D. G. Nocera, *J. Am. Chem. Soc.* **2009**, *131*, 2615.
[50] R. Abe, M. Higashi, K. Domen, *J. Am. Chem. Soc.* **2010**, *132*, 11828.
[51] H. Jun, B. Im, J. Y. Kim, Y.-O. Im, J.-W. Jang, E. S. Kim, J. Y. Kim, H. J. Kang, S. J. Hong, J. S. Lee, *Energy Environ. Sci.* **2012**, *5*, 6375.
[52] S. Ida, K. Yamada, T. Matsunaga, H. Hagiwara, Y. Matsumoto, T. Ishihara, *J. Am. Chem. Soc.* **2010**, *132*, 17343.
[53] a) G. Kresse, J. Furthmuller, *Phys. Rev. B* **1996**, *54*, 11169; b) G. Kresse, J. Furthmuller, *Comput. Mater. Sci.* **1996**, *6*, 15.
[54] Y.-S. Kim, C. H. Park, *Phys. Rev. Lett.* **2009**, *102*, 086403.